Oxygen point defect accumulation in single-phase UO_{2+x}

Raul I. Palomares, Marshall T. McDonnell, Li Yang, Tiankai Yao, Jennifer E. S. Szymanowski, Joerg Neuefeind, Ginger E. Sigmon, Jie Lian, Matthew G. Tucker, Brian D. Wirth, and Maik Lang

Phys. Rev. Materials **3**, 053611 — Published 31 May 2019

DOI: 10.1103/PhysRevMaterials.3.053611

Oxygen point defect accumulation in single-phase UO_{2+x}

Raul I. Palomares[1], Marshall T. McDonnell[2], Li Yang[1], Tiankai Yao[3], Jennifer E.S. Szymanowski[4], Joerg Neuefeind[2], Ginger E. Sigmon[4], Jie Lian[3], Matthew G. Tucker[2], Brian D. Wirth[1], Maik Lang[1]

[1] *Department of Nuclear Engineering, University of Tennessee, Knoxville, Tennessee, 37996*

[2] *Neutron Scattering Division, Oak Ridge National Laboratory, Oak Ridge, Tennessee, 37831*

[3] *Department of Mechanical, Aerospace, and Nuclear Engineering, Rensselaer Polytechnic Institute, Troy, New York*

[4] *Department of Civil and Environmental Engineering and Earth Sciences, University of Notre Dame, Notre Dame, Indiana 46556*

Keywords: UO_2, oxidation, interstitials, diffraction, total scattering, pair distribution function, reverse Monte Carlo, molecular dynamics

Abstract

$UO_{2.07}$ was characterized using neutron total scattering in order to elucidate defect morphology in the low oxygen-to-metal regime ($x < 0.125$ for UO_{2+x}). Data were collected at temperatures (600 °C and 1000 °C) coinciding with the single-phase UO_{2+x} region of the established phase diagram, and results were compared with data of stoichiometric UO_2 collected at near-identical temperatures. Experimental data were modeled and interpreted using a holistic approach employing a combination of analyses that characterized multiple spatial length scales. Preferential modeling of long-range atomic arrangements with Rietveld refinement suggests the existence of primarily mono-interstitials in $UO_{2.07}$, whereas preferential modeling of short-range atomic structures with small-box pair distribution function (PDF) refinement indicates the presence of defect clusters in $UO_{2.07}$. Simultaneous modeling of multiple length scales using complementary reverse Monte Carlo (RMC) and molecular dynamics (MD) methods confirms that excess oxygen atoms in $UO_{2.07}$ exist as small defects, such as mono-interstitials and di-interstitials. RMC and MD results agree with diffraction analysis but differ significantly from small-box PDF refinements, which may be related to a lack of intermediate- and long-range structural information gained from the small-box PDF refinement procedure. Employing a combination of analysis methods with varying length-scale sensitivities enabled more accurate assessment of the UO_{2+x} defect structure. Our findings provide experimental support for previously predicted di-interstitial defect morphologies in UO_{2+x} that highly influence the accurate prediction of bulk physiochemical properties of UO_{2+x}, such as oxygen diffusivity.

1. Introduction

Uranium dioxide is of primary technological importance as a nuclear fuel material. A unique feature of the uranium oxide system is the high degree of off-stoichiometry that the material exhibits upon varying oxygen partial pressure and temperature, such as under off-normal operating conditions. For example, there exist approximately 20 unique compositions and phase mixtures between UO_2 and U_3O_8, the most stable oxidation product in dry air at ambient pressure, with the total number remaining subject of debate [1, 2].

Oxidation of UO_2 is an exothermic process that proceeds largely through the incorporation of oxygen atoms into the UO_2 matrix. Inspection of the UO_2 fluorite structure (space group *Fm*-3*m*) would suggest that excess oxygen atoms occupy large octahedral holes in

order to minimize Coulombic forces. However, numerous experimental [3-9] and computational [10-17] studies have shown that excess oxygen atoms are not distributed at random among octahedral sites, but rather form clustered defects with neighboring lattice oxygens as a result of electronic structure effects (Figure 1). Modern *ab initio* density functional theory (DFT) studies have shown that 2*p* orbitals of interstitial oxygens can hybridize with 5*f* orbitals of nearby uranium atoms, thus decreasing band energy and yielding an attractive potential [18]. Defect clustering in oxidized UO_2 is therefore envisioned as a dynamic competition and balance between repulsive Coulomb forces and attractive hybridization effects.

Point defects are relatively small and diffuse in low concentrations but can highly influence bulk phase stability when clustered and ordered over long spatial scales. Excess oxygen interstitials at low oxygen-to-metal ratios (O:M) are theorized to exist largely as mono-interstitials and small clustered defects, such as di-interstitials (Figure 1) [19, 20]. Upon increasing interstitial concentration, defect clustering intensifies and interstitials tend to form larger cuboctahedral-type defects [21]. At even higher concentrations (UO_{2+x} with $x \sim 0.24$), cuboctahedra order over long spatial length scales to form the basis for U_4O_9-type phases, as confirmed experimentally [9]. What remains unclear is the underlying mechanism by which smaller mono- and di-interstitial defects transition to larger cuboctahedral clusters, and how defect morphology is affected by temperature. Recent theoretical findings outline a mechanism by which di-interstitials progressively agglomerate to form cuboctahedra [16]; however, the presence of di-interstitials has yet to be confirmed experimentally owing to the diffuse nature of these miniscule defects.

Experimental crystallographic studies of oxidized uranium oxide in the low-to-mid O:M regime (UO_{2+x} with $0 < x < 0.125$) are currently limited to findings from neutron diffraction, which is sensitive to low-*Z* oxygen atoms. Studies performed by Willis and Murray on UO_{2+x} (x = 0.11-0.13) at 700-800 °C show that excess oxygen in single-phase UO_{2+x} favor two unique interstitial sites displaced along <110> and <111> directions from large octahedral holes in the fluorite structure (O' and O''-type interstitials, respectively) (Figure 1) [4, 5, 7]. O' and O''-type interstitials form in equal concentrations to yield the so-called 2:2:2 Willis-type defect cluster. Experimental findings from Willis, although reproducible [4, 5], remain at odds with theoretical models, which consistently show that 2:2:2 defect configurations are unstable and decompose into smaller di-interstitial defects upon structural relaxation [14, 15].

A potential explanation for this discrepancy was derived from high-temperature *ab initio* molecular dynamics simulations, which show that 2:2:2 configurations are low-energy transition states that arise as di-interstitials migrate throughout the material [15]. This concept of low-energy migration states is not unique to 2:2:2 defects and has large implications for the prediction of bulk physical properties. *Ab initio* studies of $UO_{2.065}$ have shown that several low-energy migration pathways are available to di-interstitials, and proper accounting of these low-energy pathways enables drastic improvements in predictive capability for the derivation of diffusion coefficients with varying O:M [14, 17]. Accurate determination of defect cluster morphology in single-phase UO_{2+x} is therefore critical not only for better predicting bulk physical properties, such as oxygen diffusivity, but also for improving nuclear fission gas release models, which rely on careful interpretation of defect migration energies [22, 23].

Here, we present results from high-temperature neutron total scattering measurements of $UO_{2.07}$ performed to elucidate defect morphology in the low O:M regime in which experimental data are currently limited. The use of neutron total scattering ensures sensitivity to both low-Z oxygen atoms and small point defects, which contribute to the diffuse component of the total scattering profile. Data were collected at temperatures coinciding with the single-phase UO_{2+x} ($UO_{2+x\,(s)}$) region of the established phase diagram (Figure 2), and results are compared to data of stoichiometric UO_2 collected at near-identical temperatures. Experimental data are modeled and interpreted using a holistic approach employing a combination of different analysis methods that characterize various spatial length scales. The materials are first characterized with Rietveld and pair distribution function (PDF) refinements to study long-range and short-range atomic ordering schemes, respectively. Data are then analyzed using a large-box, reverse Monte Carlo (RMC) method to model both short and long length scales simultaneously. RMC results are compared to molecular dynamics (MD) simulations in order to investigate effects of defect cluster morphology and nano-domain formation.

2. Methodology

Uranium oxide samples were produced from microcrystalline UO_{2+x} (~$UO_{2.16}$) powder purchased from International Bio-analytical Industries Inc. USA. The feedstock material was first converted into nanocrystalline UO_{2+x} powder by high energy ball milling prior to pelletization by spark plasma sintering (SPS). Two dense pellets (> 95 % theoretical density) were prepared by SPS at

1300 °C for either 5 or 30 minutes under a pressure of 40 MPa using graphite dies. The use of graphite dies ensured that UO_{2+x} was reduced *in situ* at high temperature, with the degree of reduction being dependent on sintering time. For example, $UO_{2.07}$ and $UO_{2.00}$ samples were obtained with sintering times of 5 minutes and 30 minutes, respectively. After sintering, the dense pellets were stored and handled exclusively in inert-gas atmosphere.

Pellets were analyzed by scanning electron microscopy (SEM) and laboratory X-ray diffraction (XRD). SEM images were collected with a Carl Zeiss Supra 55 field emission SEM instrument and XRD patterns were recorded using a Panalytical X'Pert instrument equipped with a Cu Kα beam (λ = 1.5406 Å). Analyses of SEM images confirmed that both pellets contained very dense microstructures with grain sizes on the order of 1-5 μm. XRD patterns demonstrated that both materials were highly crystalline with reflections consistent with the cubic fluorite structure and no secondary phases. After SEM and XRD characterization, the dense pellets of UO_2 and $UO_{2.07}$ were crushed into microcrystalline powders in inert-gas atmosphere using an agate mortar and pestle. The microcrystalline powders were subsequently loaded into thin-walled, quartz nuclear magnetic resonance (NMR) tubes that were mounted inside vanadium cans. The vanadium cans were sealed inside the glovebox and removed immediately prior to each neutron scattering experiment.

Neutron total scattering measurements were performed at the Nanoscale Ordered MAterials Diffractometer (NOMAD) instrument of the Spallation Neutron Source (SNS) at Oak Ridge National Laboratory. Data were collected for 30 minutes at each temperature point using an Institut Laue-Langevin (ILL)-type vacuum furnace. UO_2 data were collected at 25, 100, 200, 300, 400, 500, 625, 750, 875, and 1000 ºC. $UO_{2.07}$ data were collected at 25, 100, 150, 200, 250, 300, 350, 425, 600 and 1000 ºC. The present study only concerns the data collected at 600, 625, and 1000 ºC in the single-phase UO_{2+x} region. Analysis and interpretation of the data collected at all other temperatures is reported elsewhere [24]. Measurements of an empty vanadium can with an empty quartz NMR tube insert were also performed at identical elevated temperatures in order to account for and subtract background signal. Extensive testing ensured that scattering intensity from the quartz NMR tube was not over- or under-subtracted from the sample data (Supplementary Materials (SM) Figure 1 [25]). All data were treated for multiple scattering [26] and absorption effects [27] and were normalized into absolute scale by taking into account

sample densities and packing fractions. Corrected total-scattering structure factors, $F(Q)$, were converted into total radial distribution functions, $G(r)$, by Fourier transform [28]:

$$G(r) = \frac{1}{(2\pi)^3 \rho_0} \int_{Q_{min}}^{Q_{max}} 4\pi Q^2 F(Q) \frac{\sin(Qr)}{Qr} \, dQ$$

where ρ_0 is the average number density of the material, Q is the scattering vector of length $4\pi\sin(\theta)/\lambda$ for a neutron of wavelength λ scattered at an angle 2θ, and r is real-space distance. Q_{min} and Q_{max} were set to 0.3 and 31.4 $Å^{-1}$, respectively. The $G(r)$ function naturally highlights atomic arrangements at very short length scales. The alternative differential correlation function, $D(r)$, representation was therefore used to provide more emphasis at higher r-values, *i.e.*, structural information at longer length scales. The $D(r)$ function is defined as [28]:

$$D(r) = 4\pi r \rho_0 G(r)$$

Stoichiometry calculations were performed by both unit cell parameter and ignition methods. The unit cell parameter method employed the empirical formula derived by Teske *et al*. [29] and utilized unit cell parameters derived from X-ray diffraction measurements of the pellets and neutron diffraction measurements of the powders. The ignition method was modeled after the procedure outlined in standard reference material ASTM C1453-00 [30]. The average of the three independent stoichiometry calculations yielded stoichiometry values (O:M) of 1.996(1) and 2.072(2) for the two samples, where uncertainties reflect propagated standard errors. Additional details regarding these calculations and the stoichiometry determination methods are reported elsewhere [24].

Rietveld refinement of the neutron diffraction patterns was performed with the *GSAS* software [31]. Instrument parameters were derived by fitting diffraction patterns of a powder Si 640e National Institute of Standards and Technology (NIST) sample. PDF analysis was performed by both small-box (*i.e.*, PDF refinement) and large-box (*i.e.*, RMC modeling) methods. Small-box PDF refinement was performed on the $D(r)$ functions with the *PDFgui* software [32]. For the refinements, UO_2 models were constructed assuming ideal fluorite structure symmetry (space group *Fm*-3*m*). Small-box $UO_{2.07}$ models were approximated by either: (1) incorporating 2 oxygen interstitials into 2^3 supercells in order to obtain an overall composition of $U_{32}O_{66}$ ($UO_{2.0625}$), or (2) incorporating 16 oxygen interstitials into 4^3 supercells in

order to obtain an overall composition of $U_{256}O_{528}$ ($UO_{2.0625}$). The positions of the interstitials in the 2^3 and 4^3 supercells were dictated by the defect model specified, as described in Section 3.2.

Large-box, reverse Monte Carlo (RMC) modeling of neutron total scattering data was performed with the *RMCProfile* software [33]. UO_2 data were modeled with 16000-atom, 10^3 supercells made up of 4000 uranium atoms, 8000 oxygen atoms, and 4000 vacancies. Vacancies were modeled as pseudo-atoms with neutron scattering lengths equal to zero. Preliminary tests with UO_2 data confirmed that vacancies order at empty octahedral sites, as in the ideal fluorite structure. Testing also showed that the presence of vacancies does not significantly influence optimized models. In the case of $UO_{2.07}$, 280 oxygen atoms were added to each 10^3 supercell at the expense of vacancies to yield an overall composition of $U_{4000}O_{8280}Va_{3720}$. The 280 oxygen atoms were initially distributed among 4000 random octahedral interstitial sites in each 10^3 supercell. Sensitivity analyses confirmed that supercell size, initial position of interstitials, and relative concentration of interstitials ($x = 0.07 \pm 0.04$ for UO_{2+x}) do not significantly affect derived defect structures (SM Figures 2-3 [25]). Each RMC simulation was performed by simultaneously fitting the experimental Bragg pattern, $G(r)$ function, and $D(r)$ function of a sample at a single temperature. Each simulation was run for at least 12 hours to allow sufficient time for structural optimization. Results reported for each sample at each temperature represent the ensemble average of at least 10 different RMC runs. RMC simulations were performed multiple times and averaged in order to mitigate uniqueness effects.

Optimized RMC configurations were subsequently used as starting structures for MD simulations. MD simulations for both UO_2 and $UO_{2.07}$ were performed at temperature (approximately 600 °C and 1000 °C) for up to 100 ps using interatomic potentials by either Basak *et al*. [34], Morelon *et al*. [35], or Cooper *et al*. [36]. Simulations were performed several times with each interatomic potential to avoid uniqueness effects (see, for example, SM Figures 13-14 [25]). Simulations were also performed at MD temperatures much lower than the experimental temperatures in order to optimize the fits of the MD models to the experimental data.

3. Results and Discussion

3.1. Neutron diffraction – average structure

UO_2 and $UO_{2.07}$ were first characterized by neutron diffraction in order to assess the influence of oxidation on the average structure and long-range atomic ordering arrangements. Prior analyses reveal that the diffraction patterns of UO_2 are well reproduced with a fluorite structural model between 25-1000 °C [24]. This is in contrast to $UO_{2.07}$, which was shown to undergo a UO_2 + α-U_4O_9 → UO_2 + β-U_4O_9 transformation at ~85 ºC and a UO_2 + β-U_4O_9 → UO_{2+x} transformation at ~500 ºC [24], in agreement with the established phase diagram [37]. These findings confirm that measurements of $UO_{2.07}$ performed at 600 °C and 1000 °C coincide with the single-phase UO_{2+x} regime of the phase diagram (Figure 2).

Rietveld refinement of the diffraction patterns collected at 600 °C, 625 °C, and 1000 °C show that both UO_2 and $UO_{2.07}$ are highly-ordered and well-reproduced by single-phase models (space group *Fm*-3*m*) with uranium and oxygen at 4*a* and 8*c* Wyckoff sites, respectively (SM Figure 4 [25]). Various defect structures [38] and U_4O_9-type phases [9] were fit to the diffraction patterns of $UO_{2.07}$ at 600 °C and 1000 °C; however, they did not yield an improvement over a simple fluorite structural model with interstitials (x = 0.07) randomly distributed among octahedral interstitial sites. The octahedral interstitial defect model consistently yielded the lowest goodness-of-fit value, R_w. These diffraction results suggest that either oxygen interstitials in $UO_{2.07}$ exist largely as randomly-dispersed mono-interstitials or diffraction analysis alone is not sensitive to interstitial arrangements in $UO_{2.07}$.

It's noted that Rietveld analysis of reciprocal-space diffraction data is not well-suited to investigate anharmonic effects, such as anisotropic displacement of anions, which are known to be significant in UO_2 (and presumably $UO_{2.07}$) and might influence defect ordering at high temperature [39]. This is because Rietveld refinement is reliant on the use of crystallography. A consequence of applying crystallographic constraints (*e.g.*, space group *Fm*-3*m*) is that isotropic atomic displacement parameters (ADPs) must be used to describe the atomic motion because atoms on special positions require certain coordinate/occupancy/ADP constraints. One way to circumvent this issue is to reduce the symmetry of the structural model. This was not attempted because all Bragg peaks were accounted for with the *Fm*-3*m* model, which indicates that defect signatures are conveyed in the diffuse scattering, which can only be interpreted with the use of real-space (*i.e.*, pair distribution function) analysis.

3.2. Small-box pair distribution function refinement – local structure

Numerous experimental [3-9] and computational [10-17] studies have shown that oxygen interstitials in single-phase UO_{2+x} are not randomly distributed among interstitial sites, as suggested by the diffraction analysis, but rather aggregate and form defect clusters. Defect clusters often incorporate excess interstitials, displaced lattice oxygens, and oxygen vacancies in very close proximity to each other (~2 Å at closest approach [4]). Therefore, short-range atomic structure modeling is needed in order to accurately evaluate the morphology of disordered atomic arrangements in UO_{2+x}. One means to probe short range atomic ordering is through the use of PDFs, which are weighted histograms of interatomic distances in a material. A prior comparison of neutron PDFs for UO_2 and $UO_{2.07}$ samples identical to the ones used in the current study showed that the local structures of the two materials are very similar and PDF signatures induced by oxygen defects are heavily suppressed by thermal disorder at high temperature [24]. In order to identify and interpret subtle changes in local structure associated with oxidation, the PDFs of $UO_{2.07}$ at 600 °C and 1000 °C were analyzed using the small-box PDF refinement method.

PDF refinement is analogous to Rietveld refinement of Bragg diffraction patterns. The small-box method employs relatively small and tunable structural models (98-atom 2^3 supercells in this case) with periodic boundary conditions to simulate a PDF in order to reproduce the experimental PDF and thus the local structure of a material. Unlike diffraction refinement, PDF refinement is sensitive to anharmonic effects, such as anisotropic displacement of anions, because the PDF is a spatial and temporal average of atomic correlations in the structure. Changes in the PDF are readily observable (assuming sufficient detector resolution) when anions displace/vibrate anisotropically because anions will be located in certain directions for longer periods of time, thus increasing/decreasing select PDF peak intensities (relative to the PDF of a purely isotropic material). These dynamic anharmonic effects are approximated by static atomic disorder (*i.e.*, reduced symmetry) in PDF refinements. PDF analysis is not suited to investigate dynamic mechanisms because the measurement is inherently time-averaged.

A total of eight atomic configurations were fit to the local structure of the experimental PDFs of $UO_{2.07}$ at 600 °C and 1000 °C. These configurations were the so-called *octahedral*, *<111> octahedral, <110> octahedral, di-interstitial, split di-interstitial, Willis 2:2:2*, *staggered*

IX4, and *stacked IX4* models. The first six aforementioned models were 2^3 supercell models and were fit to the PDF range 1 Å < r < 11 Å. The latter two (*staggered IX4* and *stacked IX4*) were represented by 4^3 supercells because more atoms were needed to both model split quad interstitial defects and to achieve an appropriate stoichiometry, as to match the stoichiometry of the experimental sample. The 4^3 models were fit to a broader range (1 Å < r < 22 Å) to match the larger size of the model. Larger defects, such as the cuboctahedral cluster, were not fit because they yield oxygen-to-oxygen correlations that are incompatible with the experimental PDF, as described in Section 3.4 and illustrated in SM Figure 15 [25].

All defect models use a fluorite structure supercell as an underlying framework. The *octahedral* model represents a fluorite structure supercell with oxygen interstitials (x = 0.07) randomly distributed among octahedral interstitial sites. The *<111>* and *<110> octahedral* models are variants of the aforementioned model in which interstitials were allowed to relax along either <111> or <110> directions from octahedral sites, respectively. The *di-interstitial* defect is illustrated by Wang *et al*. [15] and contains two interstitials located at the centers of two adjacent oxygen cubes. The split di-interstitial defect is described in detail by Andersson *et al*. [14] and contains three interstitials offset along <111> directions and centered around a single vacancy. The *Willis 2:2:2* is made up of two oxygen vacancies, two <111>-type interstitials, and two <110>-type interstitials as described by Willis [5]. The IX4 defect is a cluster of two split di-interstitial defects that are inverted from eachother and is also known as a split quad interstitial defect. The *staggered* and *stacked* variants indicate how IX4 clusters are arranged in the 4^3 supercells. These two models are illustrated in SM Figure 17 [25]. The di-interstitial, split di-interstitial, and Willis defects are illustrated in Figure 1. Agreement between the fitted models and experimental data was assessed using goodness-of-fit (R_w) values, which quantify discrepancies between models and experimental data. Lower R_w values indicate better fits to data.

Results from PDF refinements (Figure 3) show that several models are competitive in best representing the local structure of single-phase $UO_{2.07}$ at 600 °C and 1000 °C. The split di-interstitial and Willis models yield the best fit to the 600 °C data whereas the IX4 models yield the lowest R_w values in the 1000 °C case. The graphical and table insets of Figure 3 illustrate the fit of the Willis defect model to the data at 600 °C and the corresponding refined positions of *O'* and *O''* interstitials of the 2:2:2 cluster as described by Willis [5]. Interestingly, the *octahedral*

model, which best fits the diffraction data, yields the worst fit to the local structure of $UO_{2.07}$. The *octahedral* model fails because it yields PDF peak intensities that are incompatible with the experimental PDF profile. This peak intensity mismatch is mitigated when interstitials deviate from the highly-symmetric 4*b* octahedral site, as demonstrated by the improved fit of the *<111>* and *<110> octahedral* models compared with the *octahedral* model.

3.3. Reverse Monte Carlo total scattering modeling – multiple length scales

Conversion of UO_2 to $UO_{2.07}$ is largely caused by the ingress of oxygen interstitials into the structure, but the specific arrangement of oxygen interstitials in single-phase UO_{2+x} remains unclear. The Rietveld diffraction analysis, which interprets long-range atomic arrangements, suggests a random distribution of mono-interstitials and negligible point defect clustering. Local-structure PDF refinement, on the other hand, indicates the presence of defect clusters. In order to more accurately assess the defect structure of $UO_{2.07}$ at 600 °C and 1000 °C, neutron total scattering data were further analyzed using the reverse Monte Carlo method [33].

The RMC method is a stochastic modeling approach capable of yielding relatively large atomic structure models (16000-atom 10^3 supercells in this case). Starting configurations were constructed using unit cell data derived from Rietveld refinement of diffraction data. The aim of the method is to maximize entropy of a given atomic ensemble within a set of constraints using stochastic atom movement and swap operations. The primary constraint and driving force is that the RMC model must reproduce corresponding experimental data. Other restrictions, such as bond valence constraints, can also be utilized to add increasing levels of detail or to make models more chemically-sensible.

RMC offers two key advantages to characterizing the defect structure of single-phase UO_{2+x}. First, the method can model Bragg patterns (reciprocal-space data) and PDFs (real-space data) simultaneously in order to obtain a model that is consistent with all length scales. Second, the method is not dependent on symmetry constraints or starting defect configuration and is therefore not subject to bias from *a priori* defect models, such as the *Willis* and split *di-interstitial* models, as is the case for the small-box PDF refinement procedure. This ensures that the optimized RMC model is derived purely from experimental data and not pre-existing models.

The RMC method was benchmarked by modeling stoichiometric UO_2. The fits to the Bragg patterns and PDFs at all temperatures (SM Figure 5 [25]) demonstrate that the optimized

models fit all data well and are therefore consistent with all length scales. Bond valence sum (BVS) analysis results (SM Figure 6 [25]) show that uranium and oxygen positions are consistent with +4 and -2 charge states, respectively, meaning that the structural models are also chemically sensible. Partial PDFs, highlighting specific bond types, show how the two sublattices evolve with temperature (SM Figure 7 [25]). At high temperature, atomic vibration intensifies and atoms increasingly deviate from ideal sites (*i.e.*, Wyckoff positions) in the fluorite structure. This increase of atomic position distributions is manifested through broadening of PDF peaks at elevated temperature. Peaks in the U-U partial PDF, which purely represents the uranium sublattice, undergo the least amount of broadening of all partial PDF peaks. This agrees with the assessment that uranium atoms are much heavier and less prone to thermally-induced disorder relative to lighter oxygen atoms, which contribute to U-O and O-O partial PDFs.

Prior studies of stoichiometric UO_2 have identified unexpected properties, such as anisotropic thermal conductivity [40] and magnetic inelastic response far above the Néel temperature [41]. One possible explanation for these findings is that UO_2 contains non-cubic local atomic arrangements. Non-cubic arrangements can manifest through, *e.g.*, tetragonal distortion of the uranium sublattice and/or non-cubic uranium polyhedra. To test for the possibility of a tetragonal distortion, optimized 10^3 supercells were collapsed into unit cells and analyzed along different orientations to check for anisotropic uranium distributions (SM Figure 8 [25]). Analyses show that distributions of uranium atoms are approximately isotropic and there is no evidence of tetragonal distortion of the uranium sublattice at 625 °C or 1000 °C. The distribution of oxygen atoms (SM Figure 8 [25]) also appears isotropic despite the anisotropic broadening of the first-nearest-neighbor (1-NN) peak of the U-O partial PDF.

Similar anisotropic peak broadening was identified in a prior neutron PDF study of UO_2 at 1000 °C and was attributed to the presence of local *Pa*-3 atomic arrangements [42]. A unique consequence of the *Fm*-3*m* to *Pa*-3 space group conversion is that the characteristic fluorite-type 1-NN U-O distance splits into two distinct U-O distances. This binary U-O distribution improves the fit of the *Pa*-3 structural model to the local structure of UO_2 because it better reproduces the experimentally-observed anisotropic peak broadening. This model differs from the RMC model, which shows no evidence of a binary U-O distribution as a possible cause of the anisotropic broadening in the present data. The RMC UO_2 model instead shows that PDF data are well reproduced assuming a broad distribution, *i.e.*, continuum, comprising a variety of U-O

distances. The observation of this continuum is enabled by the relatively large sampling size (16000 atoms) of the RMC model. In order to assess effects of starting configuration, the RMC modeling procedure was repeated using a supercell with atoms initially arranged with *Pa*-3 symmetry. Test results showed that both *Fm*-3*m* and *Pa*-3 starting configurations converge to very similar atomic configurations wherein the 1-NN U-O peak comprises a continuum of U-O distances. This confirms that it is possible to reproduce the experimental data assuming a broad distribution (*i.e.*, continuum) of U-O distances instead of two discrete U-O distances. If local *Pa*-3 atomic arrangements are present in UO_2, they must exist in the form of modulated nano-domains, as previously postulated [43]. Further consideration of nano-domains is presented in Section 3.4. Results for UO_2 data collectively show that the RMC procedure yields robust large-box models that are chemically-sensible and consistent with all length scales.

The procedure for modeling $UO_{2.07}$ was identical to that of UO_2 except that the starting configurations each contained 280 extra oxygen atoms randomly dispersed among octahedral interstitials sites to yield an overall O:M of 2.07. Modeling results show that the optimized configurations for UO_2 and $UO_{2.07}$ are very similar at both 600 °C (Figure 4) and 1000 °C (SM Figure 9 [25]). As is the case for UO_2, optimized $UO_{2.07}$ models are consistent with all length scales and yield BVS results that are consistent with the presence of mostly U^{4+} and O^{2-} ions (SM Figure 6 [25]). The mean valence of uranium atoms is slightly shifted to a higher value as compared with UO_2, consistent with the expected partial oxidation of U^{4+} to U^{5+} upon ingress of oxygen into the structure. The key difference between UO_2 and $UO_{2.07}$ results is the presence of a small O-O correlation at ~2 Å in the $UO_{2.07}$ partial PDF (Figure 4d). Inspection of the $G(r)$ fits suggests that this simulated correlation arises as a means to reproduce the low-r shoulder of the first peak in the experimental PDF of $UO_{2.07}$. Extensive testing and sensitivity analyses confirm that this very subtle shoulder is a true feature of the experimental PDF and is not an artifact from data reduction (see SM Figure 1 [25] and associated figure caption for details).

The correlation at ~2 Å comprises the shortest inter-oxygen distances in the material and is therefore attributed to oxygen interstitials in the supercell. Bond vector analysis of all O-O pairs with interatomic distances between 1.9 and 2.1 Å shows that these O-O pairs are primarily oriented along <111>-type directions (Figure 5a-c). Visual inspection of these defects in the supercells reveals that these <111> O-O pairs primarily consist of one lattice oxygen and one oxygen interstitial. However, each interstitial can form between one to four 2-Å O-O pairs with

neighboring lattice oxygens (Figure 5d-f). These defects closely resemble mono-interstitials because each interstitial is almost always located near an octahedral interstitial site, and interstitials do not appear in very close proximity to other interstitials.

The key distinguishing features of these point defects are the very unique inter-oxygen distance (~2 Å) and the <111> orientation of octahedral interstitials with respect to neighboring lattice oxygens. Optimized RMC models of $UO_{2.07}$ at 600 °C and 1000 °C are highly disordered as a result of thermal effects. It is therefore difficult to determine if lattice oxygen atoms contributing to 2-Å O-O pairs are significantly displaced from ideal 8*c* Wyckoff sites or if interstitials are significantly displaced from octahedral interstitial sites. The preferential orientation of short O-O pairs along <111> directions may be caused by the inherent anisotropic vibration of anions. Lattice oxygens in the UO_2 fluorite structure are located at the centers of uranium tetrahedra and are more likely to vibrate along the four <111> directions towards octahedral interstitial sites rather than towards uranium neighbors. This assessment, coupled with the RMC results, suggests that excess oxygens in $UO_{2.07}$ primarily exist as mono-interstitials, and the distance of closest approach between interstitials and neighboring lattice oxygens is ~2 Å. This value is notable as it is the distance of closest approach reported for O'-type interstitials of the 2:2:2 Willis defect [4].

A limitation of the current RMC modeling approach is that electronic structure effects, which are key driving forces for defect clustering in UO_{2+x}, are not modeled explicitly, but instead approximated using soft, chemical, BVS constraints. In order to assess the effects of the BVS approximation, RMC modeling was performed with and without BVS constraints. Results show that simulations performed without BVS constraints also yield predominantly mono-interstitials and the formation of a small O-O correlation at ~2 Å (SM Figure 3e [25]), albeit with broader and unrealistic uranium valence distributions. This demonstrates that the key aspects of the $UO_{2.07}$ RMC defect model are robust and reflect the true atomic scattering profile of the material. Application of BVS constraints merely makes the models more chemically-sensible and does not influence point defect morphology in the models.

3.4. Molecular dynamics – nano-domain effects

RMC models show negligible point defect clustering in $UO_{2.07}$ and indicate the presence of smaller defects, such as mono-interstitials. However, RMC models are prone to artificially-

broadened atomic distributions because the procedure inherently maximizes atomic disorder. It is possible that maximizing disorder inhibits the stability of larger clusters, such as the 2:2:2 Willis and split di-interstitial defects, in the simulation supercells. Current versions of the RMC software are also incapable of simulating phase mixtures induced by co-existing nano-domains. This means that RMC simulations can potentially yield a hybrid structure when the true defect structure is instead a mixture of tessellated defect-rich and defect-free nano-domains. MD simulations using interatomic potentials were applied to the optimized RMC configurations in order to investigate these possibilities and to assess how different defect clusters and defect structures affect the simulated diffraction pattern and PDF of $UO_{2.07}$.

MD simulations were performed at temperature (approximately 600 °C and 1000 °C) using the optimized 10^3 RMC models as starting configurations. Simulations were performed using either a Basak [34], Morelon [35], or Cooper [36] potential, which are denoted $Potential_{Ba}$, $Potential_{Mo}$, and $Potential_{Co}$, respectively. Figure 6 shows the MD configurations, simulated PDFs, and simulated Bragg patterns for $UO_{2.07}$ after running for 50 ps at approximately 600 °C. MD data for $UO_{2.07}$ at 1000 °C show qualitatively similar behavior and are presented in SM Figure 11 [25]. A comparison of the simulated data to the experimental data shows that $Potential_{Mo}$ and $Potential_{Co}$ configurations best reproduce the experimental Bragg pattern of $UO_{2.07}$ despite having very different defect structures (see Figure 6f-h and SM Figure 13 [25]). $Potential_{Mo}$ configurations contain mostly mono-interstitials and small di-interstitials whereas $Potential_{Ba}$ and $Potential_{Co}$ models incorporate larger cubocahedral-type defect clusters (SM Figure 12 [25]). Experimental PDFs are also reproduced well by both $Potential_{Mo}$ and $Potential_{Co}$ (SM Figure 14 [25]); however, $Potential_{Mo}$ yields the only configuration that adequately fits the very local structure of the material ($r < 3$ Å) (SM Figure 15 [25]). Fit quality in this region is dictated by the shapes and relative peak intensities of the first two PDF peaks. The arrangement of oxygen atoms in cuboctahedral clusters ($Potential_{Co}$) causes a sharp increase in PDF peak intensity near 2.6 Å, which is incompatible with the experimental PDF (SM Figure 15 [25]). This is in contrast to smaller mono- and di-interstitial defects ($Potential_{Mo}$) that cause subtle peak broadening, as is observed experimentally. PDF peak intensity from smaller defects is more homogeneously distributed between 2-3 Å, thus better emulating the asymmetric character of the first two peaks in the experimental PDF (SM Figure 15 [25]).

Of the three interatomic potentials used, $Potential_{Mo}$ results are also most qualitatively similar to the results obtained from RMC, which is to be expected since both models contain smaller point defects. This differs from the models derived from $Potential_{Ba}$ and $Potential_{Co}$, which yielded larger cuboctahedral defects. Each cuboctahedral cluster incorporates 4-5 oxygen interstitials whereas mono-interstitials and di-interstitials only require 1 and 2 oxygen interstitials, respectively. Considering that all 10^3 atomic configurations contain an identical number of oxygen atoms, $Potential_{Ba}$ and $Potential_{Co}$ configurations more closely resemble two-phase models that contain defect-rich (*i.e.*, areas of strongly clustered defects) and defect-deficient domains. This domain-like patterning is observed as texturing of light and dark regions in Figures 6b and 6d. This behavior contrasts with the configurations derived from $Potential_{Mo}$ and RMC, which are best described as single-phase models that contain smaller, diffuse point defects and yield more homogeneous atomic distributions (Figures 6a and 6c).

MD findings confirm that experimental data are best reproduced by structural models in which excess oxygen form smaller, diffuse defects. Models containing large defect clusters and domain-like patterning are incompatible with the experimental data. Optimized RMC configurations demonstrate that excess oxygen atoms exist mostly as mono-interstitials with rare instances of di-interstitials. However, $Potential_{Mo}$ configurations show that experimental data can also be adequately reproduced with moderate concentrations of di-interstitials relative to mono-interstitials. Collectively, RMC and MD results indicate that excess oxygen atoms in single-phase UO_{2+x} in the low O:M regime ($x \rightarrow 0$) exist predominantly as mono-interstitials and di-interstitials, which supports findings from numerous DFT studies. Rudimentary analysis of 15 different MD configurations obtained using $Potential_{Mo}$ at temperatures between 300 °C and 600 °C suggest that approximately 10-20% of excess oxygen in $UO_{2.07}$ forms di-interstitials and the remainder remains in the form of mono-interstitials (SM Figure 16 [25]).

RMC and MD results qualitatively agree with the Rietveld diffraction analysis results, but differ significantly from the small-box PDF refinement results that predict the presence of larger defect clusters. This discrepancy can be explained by spatial length scale considerations. Small-box refinements emphasize local structure more heavily than intermediate- and long-range atomic ordering. Small-box models can only simulate long-range atomic ordering through the use of periodic boundary conditions or very large supercells, which increase complexity and reduce computational modeling efficiency. RMC and MD methods inherently model a larger

system size, thus directly modeling both short and long-range interatomic interactions and correlations. This suggests that the mono-interstitial/di-interstitial model is not only influenced by short-range atomic arrangements, but also by the ordering scheme of atoms and defects over longer length scales.

Future studies of point defect clustering should emphasize modeling of multiple length scales in order to derive more robust structural models. As demonstrated in this study, selective modeling of either short- or long-range atomic ordering can lead to inconsistent results. UO_{2+x} defect models may also benefit from explicit electronic structure modeling. Recent studies have demonstrated the potential to couple RMC with *ab initio* DFT to simultaneously model atomic and electronic structures [44]. Further development, optimization, and eventual application of this modeling method may potentially yield new insights into the complex interplay between atomic-scale defect behavior and bulk physiochemical properties in UO_{2+x}.

4. Conclusions

$UO_{2.07}$ was studied using neutron total scattering in order to elucidate defect morphology in the low O:M regime. Data were collected at temperatures coinciding with the single-phase UO_{2+x} region of the established phase diagram (600 °C and 1000 °C), and results were compared to data of stoichiometric UO_2 collected at near-identical temperatures. Experimental data were analyzed and interpreted using a holistic modeling approach employing a combination of different analyses that characterize various spatial length scales of the materials. Modeling of long-range atomic arrangements with Rietveld refinements of diffraction data suggests the existence of mono-interstitials in $UO_{2.07}$ whereas modeling of short-range atomic structures with pair distribution function (PDF) refinements indicates the presence of defect clusters in $UO_{2.07}$. Simultaneous modeling of multiple length scales using complementary reverse Monte Carlo (RMC) and molecular dynamics (MD) methods confirms that excess oxygen atoms in $UO_{2.07}$ primarily exist as small defects, such as mono-interstitials and di-interstitials. RMC and MD results agree with Rietveld results but differ significantly from PDF refinement results, which may be related to the lack of emphasis on the intermediate- and long-range structural information gained from the small-box PDF refinement procedure. Employing a combination of analysis methods with varying length-scale sensitivities enabled more accurate assessment of the UO_{2+x} defect structure. These findings provide experimental support for previously-predicted di-

interstitial defect morphologies in UO_{2+x} that highly influence the accurate prediction of bulk physiochemical properties, such as oxygen diffusivity.

Acknowledgements

This research was partially supported by the Office of Basic Energy Sciences of the U.S. Department of Energy as part of the Materials Science of Actinides Energy Frontier Research Center (DE-SC0001089). This work was partially funded by the University of Tennessee's Science Alliance Joint Directed Research Development program; a collaboration with Oak Ridge National Laboratory. LY and BW acknowledge support by the U. S. Department of Energy (DOE), Office of Nuclear Energy (NE) and Office of Science (SC), Office of Advanced Scientific Computing Research (ASCR) through the Scientific Discovery through Advanced Computing (SciDAC) program. JL acknowledges the financial support from the U.S. Department of Energy, Office of Nuclear Energy under a Nuclear Engineer University Program (award number: DE-NE0008440). R.I.P. acknowledges support from the U.S. Department of Energy (DOE) National Nuclear Security Administration (NNSA) through the Carnegie DOE Alliance Center (CDAC) under grant number DE-NA-0002006. The research at ORNL's Spallation Neutron Source was sponsored by the Scientific User Facilities Division, Office of Basic Energy Sciences, U.S. Department of Energy.

Figure Captions

Figure 1: Select oxygen defect cluster morphologies proposed to exist in single-phase UO_{2+x} by various researchers. Simple-cubic oxygen sublattices are shown in brown and lattice uranium atoms are shown as blue spheres. (b) A simple di-interstitial cluster comprises two neighboring octahedral interstitials separated along a <110> direction (*red spheres*). (a) These octahedral interstitials can displace along <110> directions (*pink spheres*; O'-type interstitials) and displace two neighboring lattice oxygens along <111> directions (*green spheres*; O''-type interstitials) to form a so-called 2:2:2 Willis-type defect cluster. (c) Alternatively, octahedral interstitials can displace along <111> directions (*green spheres*) and displace a neighboring lattice oxygen along a <111> direction (*green sphere*) to form a split di-interstitial cluster. Split di-interstitial clusters can further chain together in pairs to form split quad interstitial (IX4) defects or agglomerate in larger numbers to form larger cuboctahedral defects with occupied or unoccupied centers.

Figure 2: Phase diagram of uranium oxide at ambient pressure adapted from reference [37]. $UO_{2+x\ (s)}$ denotes the single-phase hyper-stoichiometric regime. Red dots indicate temperatures and O:M values at which neutron total scattering measurements were performed. Blue triangles illustrate the region investigated by Willis and Murray using single-crystal neutron diffraction [4, 5].

Figure 3: Goodness-of-fit, R_w, for different defect structural models fitted to the pair distribution function, $D(r)$, of $UO_{2.07}$ at 600 ºC and 1000 ºC. The IX4, split di-interstitial, and 2:2:2 Willis-type defect models yield similar fits to the experimental data, as illustrated by the low R_w values. The IX4 models yield the lowest R_w values in fitting $UO_{2.07}$ at 1000 ºC, while the split di-interstitial and Willis models yield slightly better fits to the 600 ºC data. The graphical inset illustrates the fit of the Willis 2:2:2 model (*red line*) to the data (*black circles*) at 600 °C. The table inset shows the displacement values [5] for <110> and <111>-type interstitials derived from the optimized Willis 2:2:2 defect models. Dashed lines are used to guide the eye.

Figure 4: Fits of optimized reverse Monte Carlo (RMC) models to experimental total scattering data of (a-b) UO_2 at 625 °C and (c-d) $UO_{2.07}$ at 600 °C. RMC models fit well to (a & c) long-range, (a & c insets) intermediate-range, and (b & d insets) short-range structures simultaneously. (b & d) UO_2 and $UO_{2.07}$ partial pair distribution functions show similar features except for a small O-O correlation present at ~2 Å in the $UO_{2.07}$ data.

Figure 5: Oxygen point defect configurations in $UO_{2.07}$ reverse Monte Carlo (RMC) models at 600 °C and 1000 °C. (a) Oxygen interstitials in the optimized RMC models cause the emergence of a small O-O correlation at ~2 Å. (b-c) Bond vector analyses show that these short (1.9-2.1 Å) O-O pairs are oriented primarily along <111> directions. The edges of these ternary plots represent the three principal cubic unit vectors (*x*, *y*, and *z*), and each data point in the ternary plot represents the orientation of a single 2-Å O-O pair in an optimized RMC model. A point lying at the center of a ternary plot represents a <111> O-O orientation, a point lying at one of the vertices represents a <100> O-O orientation, a point lying at a leg midpoint represents a <110> O-O orientation, etc. The color of the point denotes the corresponding distance for the O-O pair. (d) Counting statistics for short O-O pairs show that each interstitial forms one to four short (1.9-2.1 Å) O-O pairs with neighboring lattice oxygens. Atomic structural models for (e) single pair and (f) 4-pair configurations show that oxygen interstitials are almost always located near octahedral interstitial sites and resemble mono-interstitials. Uranium atoms, oxygen atoms at lattice sites, and oxygen atoms forming short O-O pairs (1.9-2.1 Å) in (e-f) are shown in grey, red, and blue, respectively.

Figure 6: Comparison of reverse Monte Carlo (RMC) and molecular dynamics (MD) models for $UO_{2.07}$ at 600 ºC. (a-d) Projections of 10^3 optimized supercells along principal axes. Uranium and oxygen atoms are shown in green and blue, respectively. (e-h) Comparisons of simulated PDFs (red lines) with experimental PDFs (black circles), and difference curves (green lines). Insets of (e-h) show simulated Bragg patterns (red lines), experimental Bragg patterns (black circles), and difference curves (green lines). MD $Potential_{Ba}$ yields the most disordered structural models that poorly reproduce all experimental data. $Potential_{Co}$ models are less disordered and contain larger defect clusters, but do not adequately reproduce the experimental PDF at low *r* values. $Potential_{Mo}$ models contain small point defects, are qualitatively similar to the RMC model, and best reproduce all experimental data, as illustrated by the low-intensity difference curves.

References

1. Burns, P.C. and G.E. Sigmon, eds. *Uranium: Cradle to Grave*. Mineralogical Association of Canada Short Course. Vol. 49. 2013.
2. Soo Kim, Y., *A thermodynamic evaluation of the U–O system from UO2 to U3O8.* Journal of Nuclear Materials, 2000. **279**(2): p. 173-180.
3. Cooper, R.I. and B.T.M. Willis, *Refinement of the structure of [beta]-U4O9.* 2004.
4. Murray, A.D. and B.T.M. Willis, *A neutron-diffraction study of anion clusters in non-stoichiometric uranium-dioxide.* Journal of Solid State Chemistry, 1990. **84**(1): p. 52-57.
5. Willis, B.T.M., *Defect structure of hyper-stoichiometric uranium-dioxide.* Acta Crystallographica Section A, 1978. **34**(JAN): p. 88-90.

6. Willis, B.T.M., *Point Defects in Uranium Dioxide.* Proceedings of the British Ceramic Society, 1964. **1**(1): p. 9-19.
7. Willis, B.T.M., *Structures of UO2, UO2+x and U4O9 by neutron diffraction.* Journal De Physique, 1964. **25**(5): p. 431-441.
8. Willis, B.T.M., *Positions of oxygen atoms in UO2.13.* Nature, 1963. **197**(486): p. 755-&.
9. Desgranges, L., G. Baldinozzi, D. Simeone, and H.E. Fischer, *Structural Changes in the Local Environment of Uranium Atoms in the Three Phases of U4O9.* Inorganic Chemistry, 2016.
10. Geng, H.Y., Y. Chen, Y. Kaneta, M. Iwasawa, T. Ohnuma, and M. Kinoshita, *Point defects and clustering in uranium dioxide by LSDA+U calculations.* Physical Review B, 2008. **77**(10).
11. Geng, H.Y., Y. Chen, Y. Kaneta, and M. Kinoshita, *Ab initio investigation on oxygen defect clusters in UO2+x.* Applied Physics Letters, 2008. **93**(20): p. 201903.
12. Andersson, D.A., G. Baldinozzi, L. Desgranges, D.R. Conradson, and S.D. Conradson, *Density Functional Theory Calculations of UO2 Oxidation: Evolution of UO2+x, U4O9-y, U3O7, and U3O8.* Inorganic Chemistry, 2013. **52**(5): p. 2769-2778.
13. Andersson, D.A., F.J. Espinosa-Faller, B.P. Uberuaga, and S.D. Conradson, *Stability and migration of large oxygen clusters in UO2+x: Density functional theory calculations.* Journal of Chemical Physics, 2012. **136**(23).
14. Andersson, D.A., T. Watanabe, C. Deo, and B.P. Uberuaga, *Role of di-interstitial clusters in oxygen transport in UO2+x from first principles.* Physical Review B, 2009. **80**(6).
15. Wang, J., R.C. Ewing, and U. Becker, *Average structure and local configuration of excess oxygen in UO2+x.* Scientific Reports, 2014. **4**.
16. Raoul, N.-H., K. Matthias, and P. Andreas, *Effects of stoichiometry on the defect clustering in uranium dioxide.* Journal of Physics: Condensed Matter, 2015. **27**(45): p. 455401.
17. Behera, R.K., T. Watanabe, D.A. Andersson, B.P. Uberuaga, and C.S. Deo, *Diffusion of oxygen interstitials in UO2+x using kinetic Monte Carlo simulations: Role of O/M ratio and sensitivity analysis.* Journal of Nuclear Materials, 2016. **472**: p. 89-98.
18. Andersson, D.A., J. Lezama, B.P. Uberuaga, C. Deo, and S.D. Conradson, *Cooperativity among defect sites in AO(2+x) and A(4)O(9) (A=U,Np,Pu): Density functional calculations.* Physical Review B, 2009. **79**(2).
19. Crocombette, J.-P., *Influence of charge states on energies of point defects and clusters in uranium dioxide.* Physical Review B, 2012. **85**(14): p. 144101.
20. Emerson, V., W. Julia, F. Michel, J. Gérald, and B. Marjorie, *DFT + U investigation of charged point defects and clusters in UO 2.* Journal of Physics: Condensed Matter, 2014. **26**(32): p. 325501.
21. Allen, G.C. and P.A. Tempest, *Ordered Defects in the Oxides of Uranium.* Proceedings of the Royal Society of London. Series A, Mathematical and Physical Sciences, 1986. **406**(1831): p. 325-344.
22. Bertolus, M., M. Freyss, B. Dorado, G. Martin, K. Hoang, S. Maillard, R. Skorek, P. Garcia, C. Valot, A. Chartier, L. Van Brutzel, P. Fossati, R.W. Grimes, D.C. Parfitt, C.L. Bishop, S.T. Murphy, M.J.D. Rushton, D. Staicu, E. Yakub, S. Nichenko, M. Krack, F. Devynck, R. Ngayam-Happy, K. Govers, C.S. Deo, and R.K. Behera, *Linking atomic and mesoscopic scales for the modelling of the transport properties of uranium dioxide under irradiation.* Journal of Nuclear Materials, 2015. **462**: p. 475-495.

23. Andersson, D.A., P. Garcia, X.Y. Liu, G. Pastore, M. Tonks, P. Millett, B. Dorado, D.R. Gaston, D. Andrs, R.L. Williamson, R.C. Martineau, B.P. Uberuaga, and C.R. Stanek, *Atomistic modeling of intrinsic and radiation-enhanced fission gas (Xe) diffusion in UO2 +/- x: Implications for nuclear fuel performance modeling.* Journal of Nuclear Materials, 2014. **451**(1-3): p. 225-242.
24. Palomares, R.I., J.E. Szymanowski, T. Yao, J. Neuefeind, G.E. Sigmon, J. Lian, and M. Lang, *Temperature-induced atomic-structure modifications in UO_2 and UO_{2+x}.* eprint arXiv:1905.01421, 2019: p. arXiv:1905.01421.
25. See Supplemental Materials (SM) at [URL inserted by publisher] for a summary of the systematic analyses performed to verify reverse Monte Carlo (RMC), and for SM Figures 1-17, which show comprehensive results from diffraction, PDF, RMC, and MD analyses.
26. Blech, I.A. and B.L. Averbach, *Multiple Scattering of Neutrons in Vanadium and Copper.* Physical Review, 1965. **137**(4A): p. A1113-A1116.
27. Rouse, K.D., M.J. Cooper, E.J. York, and A. Chakera, *Absorption corrections for neutron diffraction.* Acta Crystallographica Section A, 1970. **26**(6): p. 682-691.
28. Keen, D., *A comparison of various commonly used correlation functions for describing total scattering.* Journal of Applied Crystallography, 2001. **34**(2): p. 172-177.
29. Teske, K., H. Ullmann, and D. Rettig, *Investigation of the oxygen activity of oxide fuels and fuel-fission product systems by solid electrolyte techniques. Part I: Qualification and limitations of the method.* Journal of Nuclear Materials, 1983. **116**(2): p. 260-266.
30. ASTM-International, *Standard Test Method for the Determination of Uranium by Ignition and the Oxygen to Uranium (O/U) Atomic Ratio of Nuclear Grade Uranium Dioxide Powders and Pellets*. 2011, ASTM: West Conshohocken, PA.
31. Toby, B., *EXPGUI, a graphical user interface for GSAS.* Journal of Applied Crystallography, 2001. **34**(2): p. 210-213.
32. Farrow, C.L., P. Juhas, J.W. Liu, D. Bryndin, E.S. Bozin, J. Bloch, T. Proffen, and S.J.L. Billinge, *PDFfit2 and PDFgui: computer programs for studying nanostructure in crystals.* Journal of Physics-Condensed Matter, 2007. **19**(33).
33. Tucker, M.G., A.K. David, T.D. Martin, L.G. Andrew, and H. Qun, *RMCProfile: reverse Monte Carlo for polycrystalline materials.* Journal of Physics: Condensed Matter, 2007. **19**(33): p. 335218.
34. Basak, C.B., A.K. Sengupta, and H.S. Kamath, *Classical molecular dynamics simulation of UO2 to predict thermophysical properties.* Journal of Alloys and Compounds, 2003. **360**(1–2): p. 210-216.
35. Morelon, N.D., D. Ghaleb, J.M. Delaye, and L. Van Brutzel, *A new empirical potential for simulating the formation of defects and their mobility in uranium dioxide.* Philosophical Magazine, 2003. **83**(13): p. 1533-1550.
36. Cooper, M.W.D., M.J.D. Rushton, and R.W. Grimes, *A many-body potential approach to modelling the thermomechanical properties of actinide oxides.* Journal of Physics: Condensed Matter, 2014. **26**(10): p. 105401.
37. Higgs, J.D., W.T. Thompson, B.J. Lewis, and S.C. Vogel, *Kinetics of precipitation of U4O9 from hyperstoichiometric UO2+x.* Journal of Nuclear Materials, 2007. **366**(3): p. 297-305.
38. Kim, J.S., Y.N. Choi, C.H. Lee, S.H. Kim, and Y.W. Lee, *Crystal Structure Analysis of Uranium Oxides.* Journal of the Korean Ceramic Society, 2001. **38**(11): p. 967-972.

39. Rouse, K.D., B.T.M. Willis, and A.W. Pryor, *Anharmonic contributions to the Debye-Waller factors of UO2.* Acta Crystallographica Section B, 1968. **24**(1): p. 117-122.
40. Gofryk, K., S. Du, C.R. Stanek, J.C. Lashley, X.Y. Liu, R.K. Schulze, J.L. Smith, D.J. Safarik, D.D. Byler, K.J. McClellan, B.P. Uberuaga, B.L. Scott, and D.A. Andersson, *Anisotropic thermal conductivity in uranium dioxide.* Nature Communications, 2014. **5**.
41. Caciuffo, R., G. Amoretti, P. Santini, G.H. Lander, J. Kulda, and P.D. Du Plessis, *Magnetic excitations and dynamical Jahn-Teller distortions in UO2.* Physical Review B, 1999. **59**(21): p. 13892-13900.
42. Desgranges, L., Y. Ma, P. Garcia, G. Baldinozzi, D. Siméone, and H.E. Fischer, *What Is the Actual Local Crystalline Structure of Uranium Dioxide, UO2? A New Perspective for the Most Used Nuclear Fuel.* Inorganic Chemistry, 2016.
43. Desgranges, L., Y. Ma, P. Garcia, G. Baldinozzi, D. Siméone, and E. Fischer Henry, *Understanding Local Structure versus Long□Range Structure: The□Case of UO2.* Chemistry A European Journal, 2018. **24**(9): p. 2085-2088.
44. Bhattarai, B., A. Pandey, and D.A. Drabold, *Evolution of amorphous carbon across densities: An inferential study.* Carbon, 2018. **131**: p. 168-174.

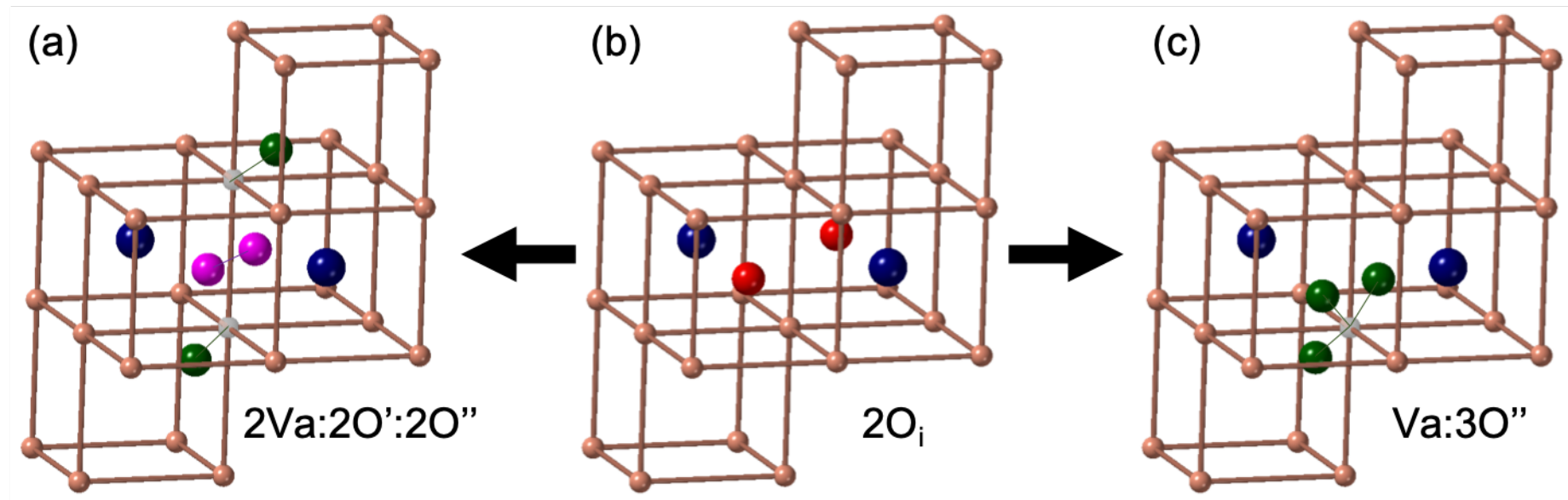
(a)
2Va:2O':2O''
(b)
2O$_i$
(c)
Va:3O''

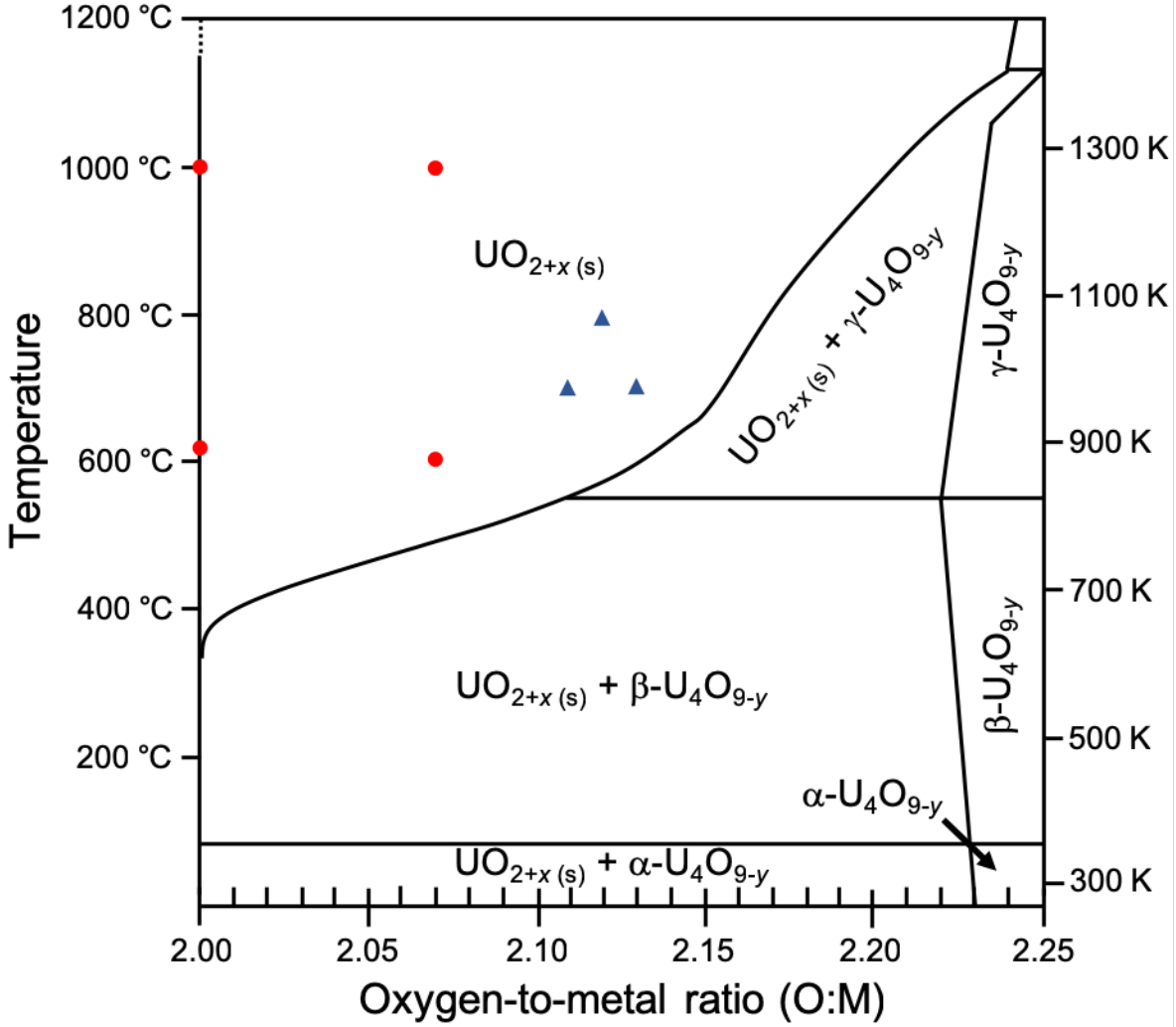
1200 °C
1000 °C
800 °C
600 °C
400 °C
200 °C
Temperature
1300 K
1100 K
900 K
700 K
500 K
300 K
$UO_{2+x\,(s)}$
$UO_{2+x\,(s)}$ + γ-U_4O_{9-y}
γ-U_4O_{9-y}
$UO_{2+x\,(s)}$ + β-U_4O_{9-y}
β-U_4O_{9-y}
α-U_4O_{9-y}
$UO_{2+x\,(s)}$ + α-U_4O_{9-y}
2.00
2.05
2.10
2.15
2.20
2.25
Oxygen-to-metal ratio (O:M)

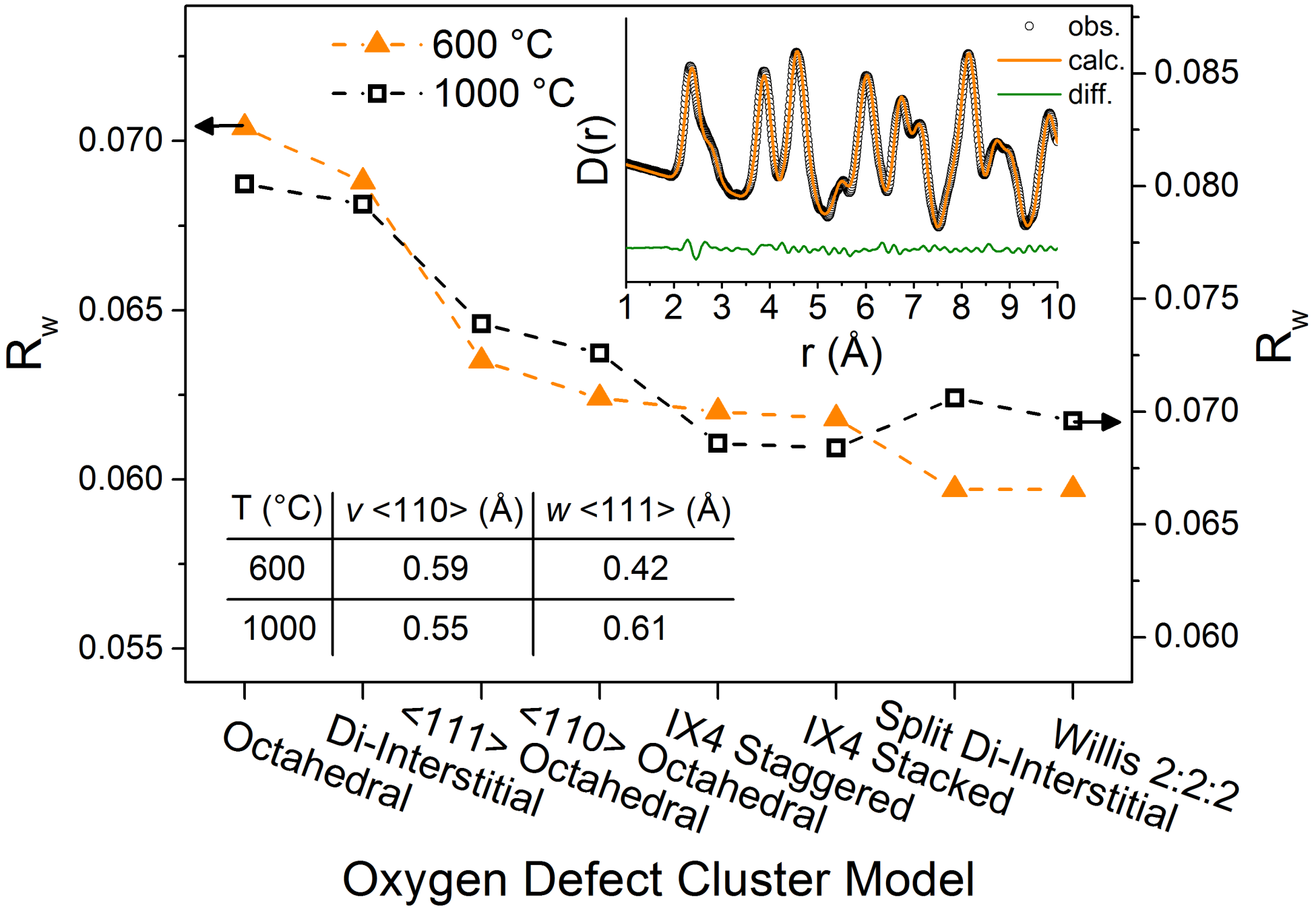
600 °C
1000 °C
obs.
calc.
diff.
D(r)
r (Å)
1 2 3 4 5 6 7 8 9 10
R_w
0.070
0.065
0.060
0.055
0.085
0.080
0.075
0.070
0.065
0.060
T (°C) | v <110> (Å) | w <111> (Å)
600 | 0.59 | 0.42
1000 | 0.55 | 0.61
Octahedral
Di-Interstitial
<111> Octahedral
<110> Octahedral
IX4 Staggered
IX4 Stacked
Split Di-Interstitial
Willis 2:2:2
Oxygen Defect Cluster Model

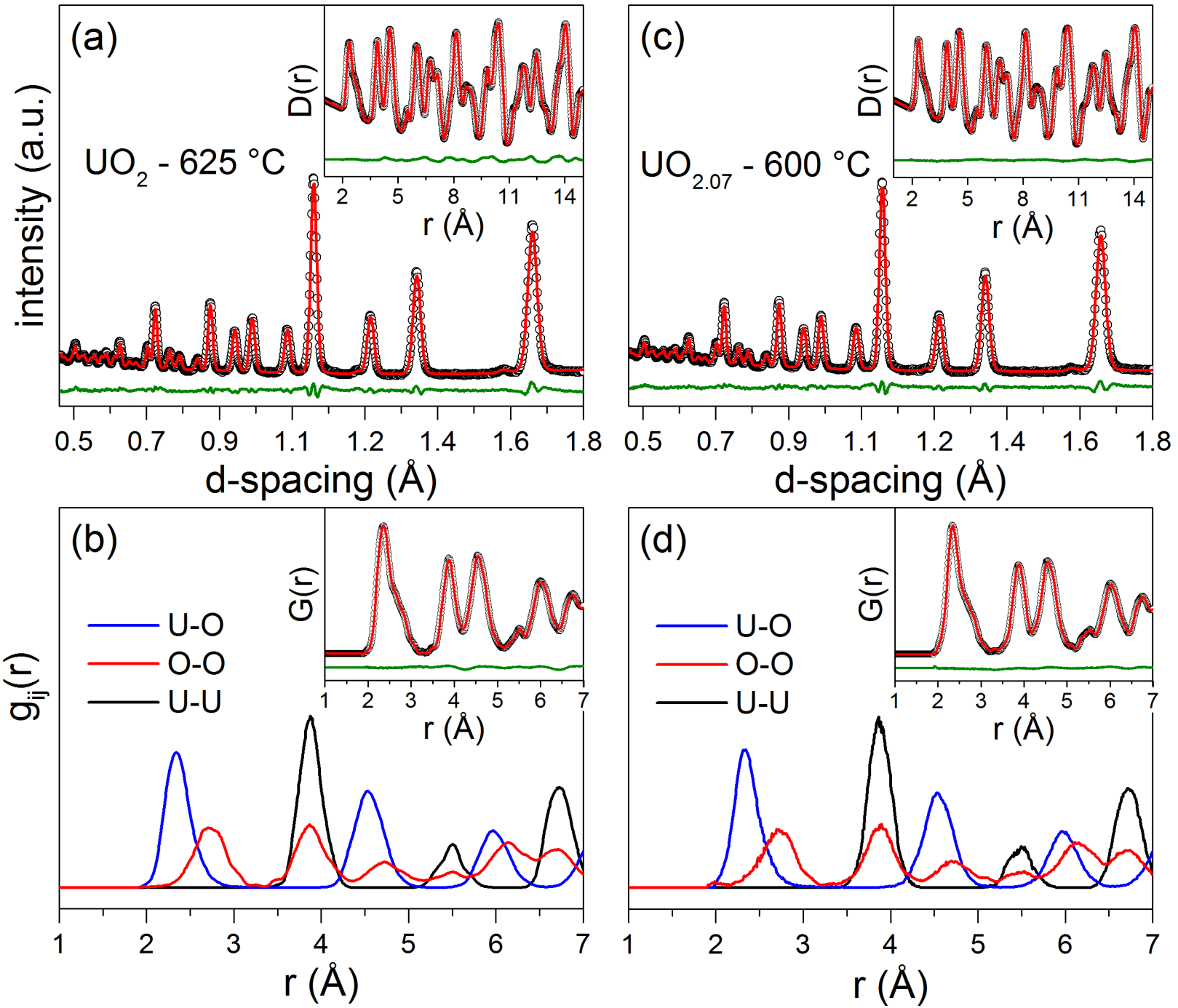
(a)
UO2 - 625 °C
intensity (a.u.)
D(r)
r (Å)
d-spacing (Å)
(c)
UO2.07 - 600 °C
(b)
U-O
O-O
U-U
gij(r)
G(r)
(d)

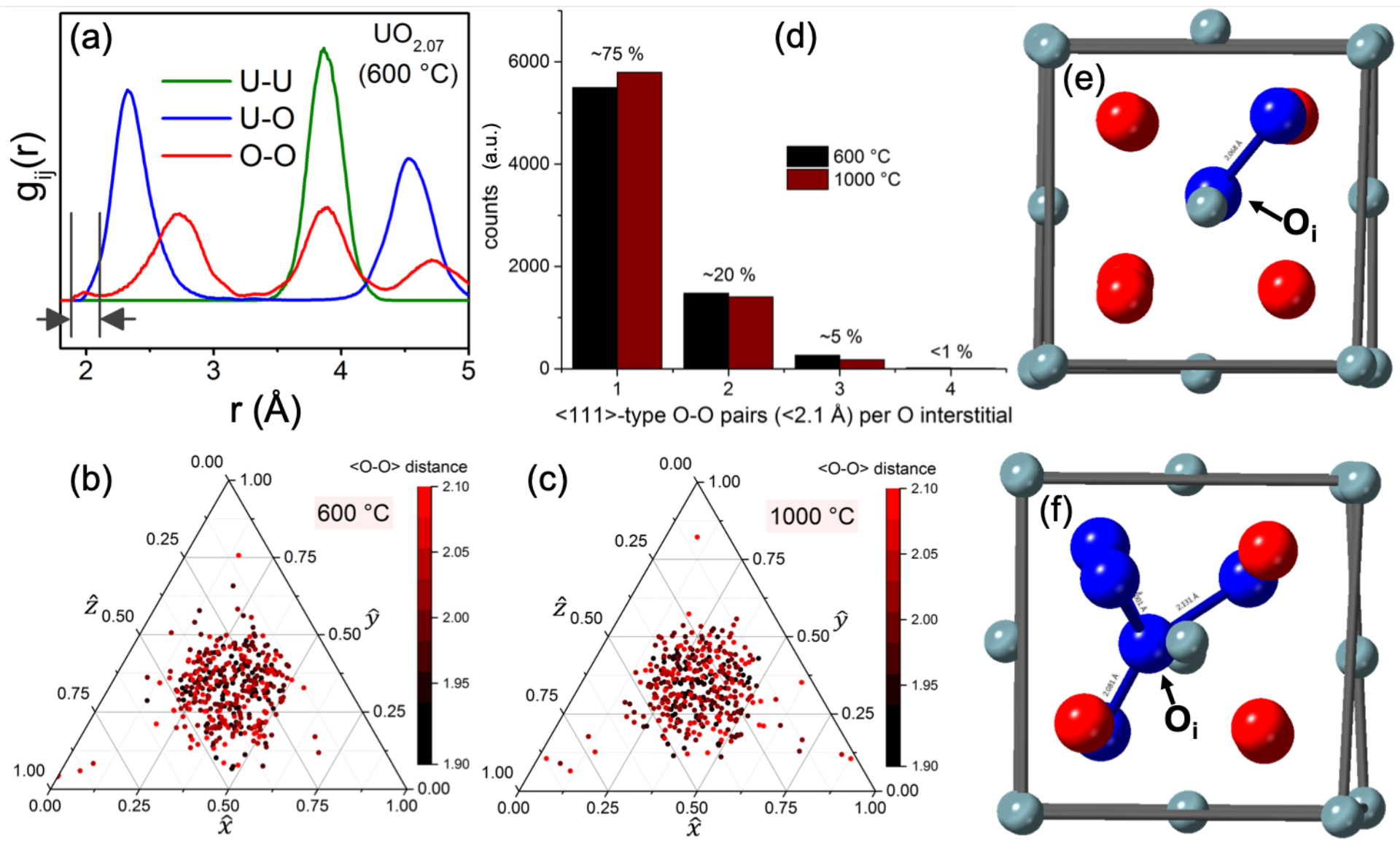
(a)
UO2.07
(600 °C)
U-U
U-O
O-O
gij(r)
r (Å)
(d)
~75 %
~20 %
~5 %
<1 %
600 °C
1000 °C
counts (a.u.)
<111>-type O-O pairs (<2.1 Å) per O interstitial
(e)
Oi
(b)
600 °C
<O-O> distance
(c)
1000 °C
(f)

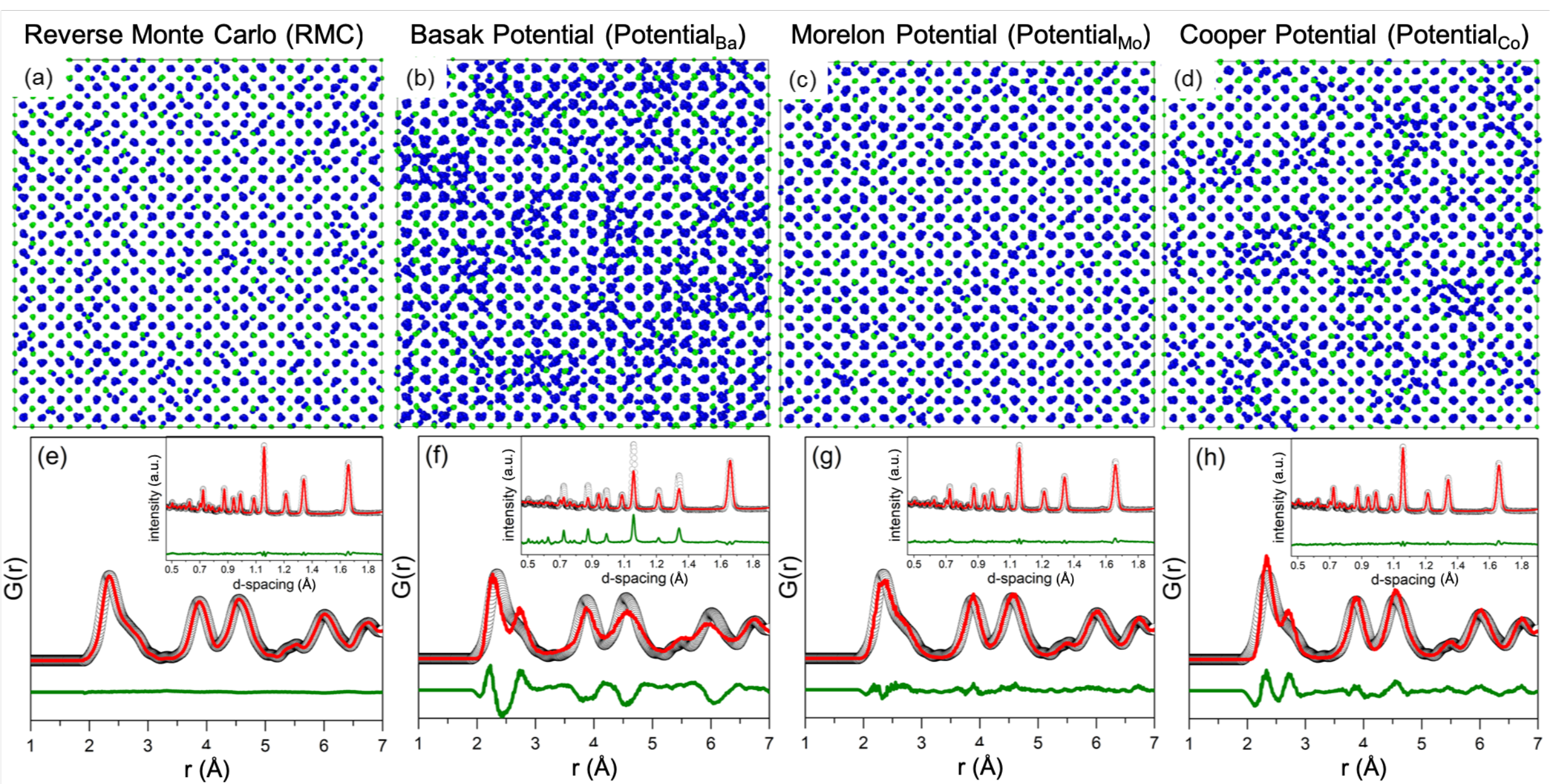
Reverse Monte Carlo (RMC)
Basak Potential (Potential$_{Ba}$)
Morelon Potential (Potential$_{Mo}$)
Cooper Potential (Potential$_{Co}$)
(a)
(b)
(c)
(d)
(e)
(f)
(g)
(h)
G(r)
r (Å)
intensity (a.u.)
d-spacing (Å)